Chinese Physics Letters

LETTER

Giant Planar Hall Effect of Unprecedented Amplitude in n-HgTe with Extremely Low Electron Density

Cite as: A.T. Lonchakov *et al*. 2026 *Chin. Phys. Lett.* **43** 110706

DOI CSTR

Recommended Articles

Planar Hall Effect in the Charge-Density-Wave $Bi_2Rh_3Se_2$

Mingju Cai, Zheng Chen, Yang Yang, Xiangde Zhu, Haoxiang Sun, Ankang Zhu, Xue Liu, Yuyan Han, Wenshuai Gao, and Mingliang Tian
Chin. Phys. Lett. **41**, (2024)

Observation of Giant Topological Hall Effect in Room-Temperature Ferromagnet $Cr_{0.82}Te$

Wei-Ting Miao, Wei-Li Zhen, Zhen Lu, Heng-Ning Wang, Jie Wang, Qun Niu, and Ming-Liang Tian
Chin. Phys. Lett. **41**, (2024)

MBE Growth and Characterization of Strained HgTe (111) Films on CdTe/GaAs

Jian Zhang, Shengxi Zhang, Xiaofang Qiu, Yan Wu, Qiang Sun, Jin Zou, Tianxin Li, and Pingping Chen
Chin. Phys. Lett. **37**, 038101 (2020)

Chiral Anomaly in Non-Relativistic Systems: Berry Curvature and Chiral Kinetic Theory

Lan-Lan Gao, and Xu-Guang Huang
Chin. Phys. Lett. **39**, 021101 (2022)

Chiral Anomaly-Enhanced Casimir Interaction between Weyl Semimetals

Jia-Nan Rong, Liang Chen, and Kai Chang
Chin. Phys. Lett. **38**, 084501 (2021)

A series journal of Chinese Physical Society distributed by IOP Publishing

Chinese Physics Letters

Chin. Phys. Lett. **43** 110706 (2026)

LETTER

DOI: 10.1088/0256-307X/43/11/110706
CSTR: 32039.14.0256-307X.43.11.110706

Giant Planar Hall Effect of Unprecedented Amplitude in n-HgTe with Extremely Low Electron Density

A.T. Lonchakov, S.B. Bobin*, and S.D. Popov

M.N. Mikheev Institute of Metal Physics of the Ural Branch of Russian Academy of Sciences, Yekaterinburg 620077, Russian Federation

*Corresponding author. Email: bobin@imp.uran.ru

We report the observation of a giant planar Hall effect in an n-HgTe single crystal with an extremely low electron density of 7.3×10^{14} cm^{-3}. Its amplitude reaches an unprecedented value of 0.9 Ohm·cm at $T = 40$ K and in a magnetic field of 10 T—to the best of our knowledge, the highest ever reported for this effect in any topological material. We attribute the strong magnetoresistance anisotropy underlying the giant planar Hall effect to the coexistence of a topological Weyl semimetal phase and a trivial gapless phase in the band spectrum of a bulk n-HgTe. The former gives rise to strong negative longitudinal magnetoresistance driven by chiral anomaly, whereas the latter leads to charge compensation-induced positive transverse magnetoresistance without saturation. We have established that it is precisely this magnetoresistance that provides the dominant contribution to the giant amplitude of the planar Hall effect. The observed giant planar Hall effect in this particular n-HgTe sample suggests that low-density mercury telluride merits further investigation as a candidate material for exploring chiral-anomaly transport and for potential sensor applications.

Introduction

The planar Hall effect (PHE) occupies a special place among galvanomagnetic phenomena. The conventional Hall effect requires a magnetic field component perpendicular to both the sample plane and the electric current. By contrast, the PHE occurs in a geometry where the applied magnetic and electric fields, as well as the induced transverse electric field, all lie in the same plane—precisely the configuration in which the ordinary Hall effect vanishes. A prerequisite for the occurrence of the PHE is the anisotropy of magnetoresistance (MR), that is the dependence of the components of the resistivity tensor on the angle θ between the magnetic field and the current direction, which may have various origins. The PHE manifests itself as characteristic π-periodic oscillations of the MR measured both transverse and longitudinal to the electric current, when the magnetic field is rotated in the sample plane. The former is commonly referred to as the planar Hall resistance $\rho_{xy}(\theta)$, and the latter as the planar anisotropic MR (AMR) $\rho_{xx}(\theta)$. Historically, the PHE was discovered as early as 1954 in n- and p-Ge crystals and was explained by the anisotropy of MR stemming from the anisotropy of the Fermi surface and relaxation time [1]. Subsequently, in addition to nonmagnetic systems with anisotropy of orbital MR caused by the Lorentz force, the PHE has been extensively studied in ferromagnetic materials with magnetic anisotropy. The generally accepted interpretation is that, in such systems, the PHE arises from a change in the spin–orbit scattering probability as the magnetization rotates in the plane together with the magnetic field relative to the current [2].

Interest in the PHE has grown significantly over the past decade, following the discovery of topological Dirac and Weyl semimetals (WSMs). In a WSM, massless Weyl fermions exist close to the Fermi level, with linear dispersion near the Weyl nodes (band touching points) [3]; Weyl nodes always come in pairs of opposite chirality. This interest has been further driven by theoretical predictions [4, 5] that the PHE emerges in topological materials from their inherent chiral anomaly and Berry curvature. The chiral anomaly, a quantum phenomenon from high-energy physics, manifests as non-conservation of Weyl fermions of a given chirality under collinear electric and magnetic fields [6]. A notable experimental achievement was our 2023 discovery of a giant PHE in an ultra-pure HgSe single crystal—a candidate for the family of the inversion-breaking WSMs [7]. The amplitude of the planar Hall resistance oscillations in this sample at $T = 80$ K reached ≈ 50 mOhm·cm in a magnetic field of 10 T, which exceeded the PHE amplitude in known topological semimetals by up to three orders of magnitude. This discovery was preceded by our observation of the chiral magnetic effect (CME) in the same sample [8]. Unlike negative longitudinal MR, which is affected by artefacts such as current jetting, the PHE is a more reliable signature of the chiral anomaly.

Beyond its fundamental role in probing the chiral anomaly and Berry curvature, the PHE is used in magnetic field sensors, magnetic nanoparticle detection, and magnetoresistive random-access memory (MRAM) devices [9–19]. PHE-based magnetoresistive sensors offer high sensitivity (down to the sub-50 nT range), excellent thermal stability, low detection limits, simple design, low cost, and compatibility with flexible and lab-on-a-chip platforms [9–12]. Elliptical PHE sensors achieve equivalent magnetic noise of order pT/√Hz [13], making them promising candidates for a range of sensing applications. In addition, PHE sensors are also well suited for detecting magnetic nanoparticles as biomarkers for ultra-early disease diagnosis [14–16] and for precisely determining magnetization direction in thin-film MRAM [17–19].

Given the giant PHE in ultrapure HgSe [7], it was of interest to test another mercury chalcogenide, n-HgTe with an extremely low electron concentration, for the PHE. The non-centrosymmetric zincblende structure, strong spin–orbit coupling, and inverted band spectrum of HgTe favour topological phases [20]. Our recent magnetotransport study of a bulk n-HgTe sample with an extremely low electron density (7.3×10^{14} cm^{-3}) provided solid evidence for the coexistence of trivial and topological phases in its band spectrum [21]. Specifically, we revealed the CME as a direct manifestation of the chiral anomaly, as well as an unconventional Hall resistance indicative of Weyl node annihilation in the quantum limit. These findings establish low-density n-HgTe as a promising platform for chiral-anomaly-driven magnetotransport. Accordingly, we selected the n-HgTe sample studied in Ref. [21] for testing the PHE. The present study should be considered an extension of Ref. [21], in which the out-of-plane magnetotransport and the chiral anomaly were investigated in detail for this sample. The work aims to detect and analyse the PHE in n-HgTe, compare its amplitude with that in HgSe [7], and

Received 2 July 2026; accepted 10 October 2026; published 5 November 2026

© 2026 Chinese Physical Society and IOP Publishing Ltd. All rights, including for text and data mining, AI training, and similar technologies, are reserved.

Check for updates

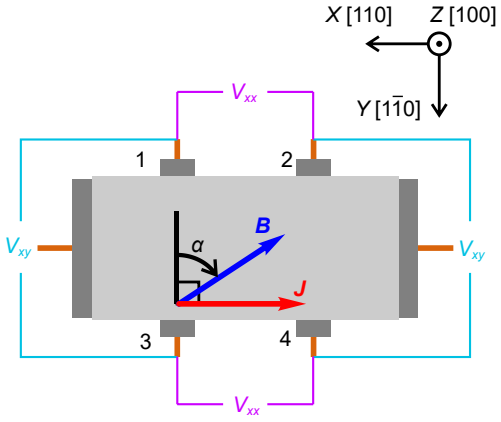

Fig. 1. Schematic representation of the PHE measurement geometry. The (100) plane of the n-HgTe sample and the crystallographic axes within it are shown.

elucidate whether the effect's origin lies in the chiral anomaly or other mechanisms. It is worth noting that, to date, only a single n-HgTe sample with an extremely low electron density has been investigated.

Experimental Details

A nominally pure n-HgTe single crystal had an electron concentration $n_e = 7.3\times10^{14}$ cm^{-3} at $T = 0.3$ K—the lowest, to the best of our knowledge, ever recorded in mercury chalcogenides. This corresponds to a Hall mobility $\mu_e = 2.7\times10^5$ cm$^2\cdot$V$^{-1}\cdot$s^{-1} and a Fermi energy $\varepsilon_F = 4.1$ meV. The mobility at $T = 80$ K was 8.5×10^4 cm$^2\cdot$V$^{-1}\cdot$s^{-1}, and the intrinsic electron concentration was 2.2×10^{17} cm^{-3}. Other electronic parameters are presented in detail in Ref. [21]. This unique sample has a long history: it was cut from a homogeneous part of an ingot grown by the Bridgman technique as early as 1979. The sample had the shape of a rectangular parallelepiped and was oriented as shown in Fig. 1. This n-HgTe sample is distinctive as one of the samples on which magnetophonon resonance was studied as early as 1988 [22]. Since then, it had undergone a long-term (over nearly forty years) procedure that can be defined as "passive annealing" [23]—storage of the sample at room temperature and normal atmospheric pressure. As a result, the concentration of both donor- and acceptor-type defects should have considerably decreased. Apparently, the very low n_e in this sample is precisely indicative of this. The dimensions of the sample were $(t\times d\times l) \approx (0.7\times1\times5)$ mm^3, where t, d, and l are the thickness, width, and length of the sample, respectively. Prior to the deposition of ohmic contacts, the sample was etched in a 5% solution of bromine in methanol for about 2 minutes. A eutectic alloy of gallium and indium with an addition of ≈ 10% silver was used as the ohmic contact material. The distance between the potential contacts was ≈ 1 mm. Planar magnetotransport was measured using the four-probe method at $T = 40$, 80, and 150 K in magnetic fields up to ±12 T. Temperature stabilization was maintained within (0.5–1) K using a special measuring cell equipped with a rotator. All magnetotransport measurements were carried out at a current of 10 mA. Figure 1 shows the sample sketch and measurement geometry, including crystallographic axes. Two important features are the following: (i) for reliability, transverse (V_{xy}) and longitudinal (V_{xx}) voltages were recorded from two pairs of contacts [(1–3), (2–4) and (1–2), (3–4) respectively)]; (ii) current contacts fully covered both sample ends to minimize the current-jetting effect [24]. The sample was rotated in the magnetic field lying in the (100) plane, over an angle α from 0 to π (Fig. 1) at both field directions, equivalent to a 0–2π rotation. The rotator design allowed α to be measured from the direction normal to the current and enabled the rotation angle to be set with an accuracy of better than 1°. The voltages from the two contact pairs differed negligibly, so the reported ρ_{xy} and ρ_{xx} are averaged over the two pairs. It should also be noted that the measurement results were reproducible to within 5% upon repeated rotations and after re-mounting the sample on the rotator stage.

Before presenting the main experimental data, we point out two potential factors that can distort the α-dependences of ρ_{xy} and ρ_{xx}. The first source of error is the contribution of the ordinary Hall effect to ρ_{xy}, arising from the presence of a magnetic field component perpendicular to the sample plane due to non-ideal sample alignment. This contribution is odd in the magnetic field. We estimate that the sample alignment inaccuracy could be approximately 0.5°, which corresponds to a perpendicular magnetic field component of about 0.09 T in a field of 10 T. The second type of error is associated with the inevitable misalignment of the Hall contacts relative to each other, which occurs during sample fabrication. The non-equipotentiality of the Hall contacts leads to a contribution from the longitudinal MR to the transverse effect, which is even in the magnetic field. These and other factors have been taken into account as described in detail in Ref. [7]. The data processing accordingly followed that procedure and is not repeated here; we present only the final results.

Experimental Results and Discussions

If a sample exhibits MR anisotropy and the magnetic field is rotated in the plane of the sample by an angle θ relative to the current direction, the resulting components ρ_{xy} and ρ_{xx} are described by the following equations [25]:

$$\rho_{xy} = -\Delta\rho\sin\theta\cos\theta, \tag{1}$$

$$\rho_{xx} = \rho_\perp - \Delta\rho\cos^2\theta, \tag{2}$$

where $\Delta\rho = \rho_\perp - \rho_\parallel$ is the PHE amplitude. The quantities $\rho_\perp$ and $\rho_\parallel$ denote the MRs when the magnetic field $\boldsymbol{B}$ is perpendicular and parallel to the electric current $\boldsymbol{J}$, respectively, while lying in the sample plane (Fig. 1). Equations (1) and (2) are universal for any type of anisotropy. Since our α is measured from the perpendicular to the electric current (Fig. 1), we replace θ with $(\pi/2-\alpha)$ in Eqs. (1) and (2). Equations (1) and (2) then become

$$\rho_{xy} = -\Delta\rho\cos\alpha\sin\alpha, \tag{3}$$

$$\rho_{xx} = \rho_\perp - \Delta\rho\sin^2\alpha, \tag{4}$$

which we will use henceforth to describe our experiment. In WSMs, the resistivity tensor can become anisotropic due to two factors: (i) the chiral anomaly, which leads to negative MR $\rho_\parallel(B)$; and (ii) the lifting of the protection against backscattering, accompanied by a large positive $\rho_\perp(B)$. Let us clarify this point. According to the quantum theory of chiral wave-packet scattering by a single impurity [26], in WSMs electrons acquire a chirality-protected side-jump shift due to their definite chirality. The theory predicts this shift to be most pronounced for large-angle scattering. The application of a magnetic field suppresses this shift, leading to a marked increase in MR.

The experimental dependences $\rho_{xy}(\alpha)$ and $\rho_{xx}(\alpha)$ for the n-HgTe sample with an extremely low electron density, measured at $T = 80$ K, are represented by symbols in Fig. 2. The angular dependences are well fitted by Eqs. (3) and (4) (solid curves in Fig. 2), with a high coefficient of determination ($R^2 = 0.9954$), indicating the good quality of the fitting. According to Eq. (3), $\rho_{xy}(\alpha)$ oscillates with a period of π, exhibiting maxima at $\alpha = \pi/4$ and $3\pi/4$ over the interval from 0 to 2π. The oscillations of $\rho_{xx}(\alpha)$ exhibit the same period but are phase-shifted by $\pi/4$ relative to $\rho_{xy}(\alpha)$. We define the PHE amplitude $\Delta\rho$ as the variation of the sinusoidal $\rho_{xy}(\alpha)$ curve from minimum to maximum according to Eq. (3), and the equal amplitude of the AMR as the variation from the peak ($\alpha = 0$) to the valley ($\alpha = \pi/2$) of the $\rho_{xx}(\alpha)$ curve according to Eq. (4). We will strictly adhere to these definitions in the analysis of the experiment and in comparing our data with the PHE in other materials. Then, at $T = 80$ K and in a field of 12 T, the experimental amplitude $\Delta\rho$ for $\rho_{xy}(\alpha)$ amounts to ≈ 185 mOhm·cm

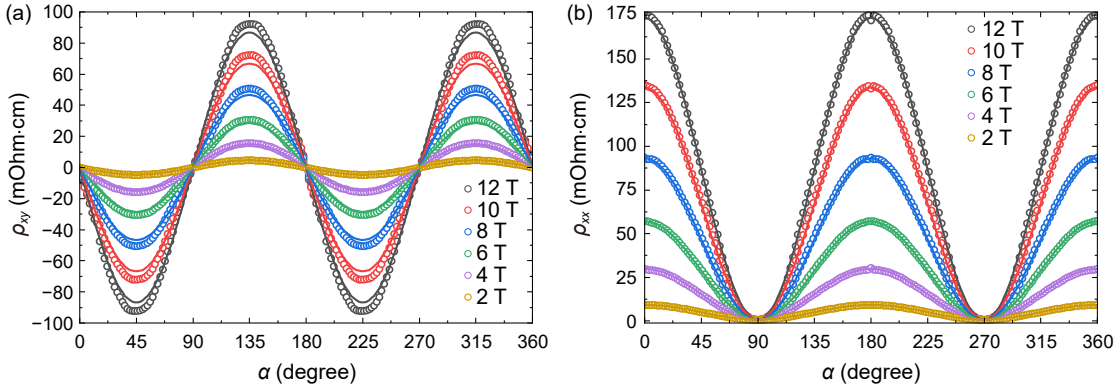

Fig. 2. Planar Hall effect in the n-HgTe sample at $T = 80$ K for different magnetic fields. Symbols: experimental angular dependences of (a) planar Hall resistivity ρ_{xy} and (b) planar anisotropic magnetoresistivity ρ_{xx}. Solid lines: fits to Eqs. (3) and (4), respectively.

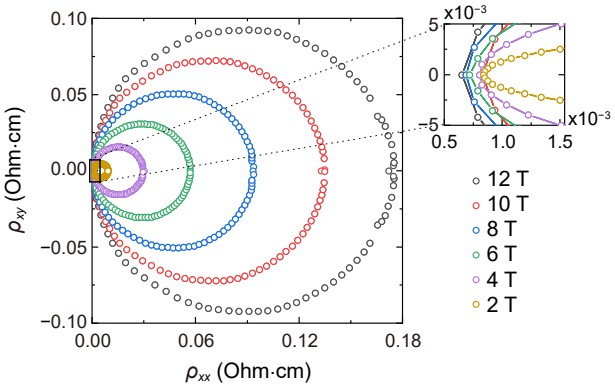

Fig. 3. Parametric plots of ρ_{xy} as a function of ρ_{xx} at $T = 80$ K for different fields.

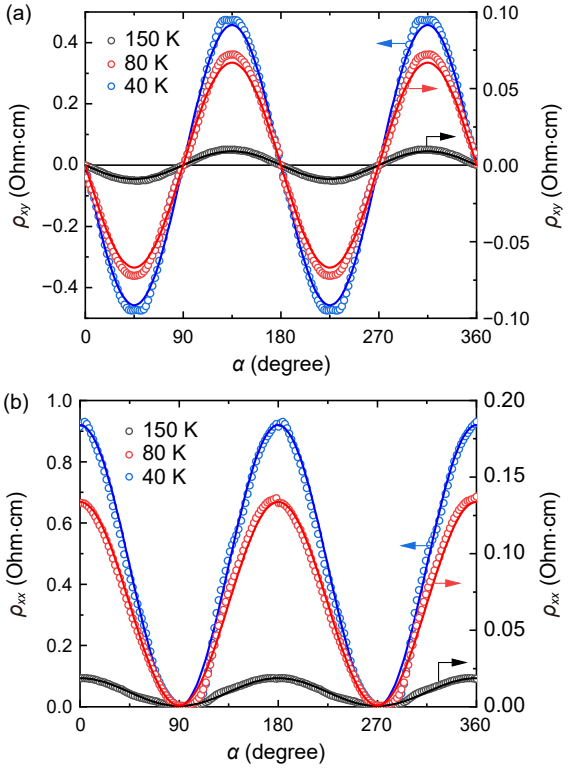

Fig. 4. Planar Hall effect in the n-HgTe sample at 10 T for different temperatures. Symbols: experimental angular dependences of (a) planar Hall resistivity ρ_{xy} and (b) planar anisotropic magnetoresistivity ρ_{xx}. Solid lines: fits to Eqs. (3) and (4), respectively.

[Fig. 2(a)], and for $\rho_{xx}(\alpha)$ to 175 mOhm·cm [Fig. 2(b)]. The amplitude obtained from fitting by Eqs. (3) and (4) is found to be somewhat smaller, equal to ≈ 173 mOhm·cm (solid curves in Fig. 2). This value is approximately 3 times larger than the PHE amplitude in ultra-pure HgSe [7] under the same experimental conditions. The data presented in Figs. 2(a) and 2(b) can be combined by plotting parametric ρ_{xy} versus ρ_{xx} curves at a fixed field B, using the rotation angle α as a parameter. The set of such parametric plots is shown in Fig. 3. For n-HgTe, the parametric dependences at different B are closed convex curves, elongated to the right along the ρ_{xx} axis and nested within each other. This elongation stems from the increase in $\rho_{\perp}(B)$ with B. Figure 3 qualitatively mirrors the pattern of parametric plots at $T = 80$ K in ultra-pure HgSe [7].

Further, as a continuation of the experiment, measurements of $\rho_{xy}(\alpha)$ and $\rho_{xx}(\alpha)$ were performed at a fixed field of 10 T and temperatures of 40 and 150 K, which differ from the "baseline" $T = 80$ K by a factor of ≈ 2. The experimental results, together with the PHE data at $T = 80$ K, are shown in Fig. 4. Remarkably, at $T = 40$ K the fitted amplitude of $\rho_{xy}(\alpha)$ and $\rho_{xx}(\alpha)$ increased by a factor of ≈ 5.5 relative to $\Delta\rho$ at $T = 80$ K, reaching an unprecedentedly high value of ≈ 0.9 Ohm·cm. The shape of the oscillations remained nearly sinusoidal, as evidenced by their fit to Eqs. (3) and (4) (solid curves in Fig. 4). The uncertainty in the absolute resistivity values is estimated to be approximately 9%, with the main contribution arising from the uncertainty in the sample geometry, while the contribution from the electrical measurements is much smaller. For the record amplitude of 0.9 Ω·cm at 40 K, this implies an uncertainty of about ±0.08 mOhm·cm. To illustrate the extraordinary magnitude of the PHE in n-HgTe at $T = 40$ K, we provide some comparisons with other topological materials. The difference turns out to be so significant that it is fully justified to compare the PHE amplitudes by order of magnitude. The amplitude we observe (~ 1 Ohm·cm) exceeds $\Delta\rho$ in the WSM GdPtBi [27] by three orders of magnitude, in TaAs [28] by four orders, in $PtBi_2$ [29] by five orders, and in WTe_2 [30] by six orders. This list can be extended to include, for example, Dirac semimetals such as $PdTe_2$ [31, 32], VAl_3 [33], $PtTe_2$ [34], and Cd_3As_2 [35], as well as topological insulators such as $NaCd_4As_3$ [36], $MnBi_8Te_{13}$ [37], Ni_3Bi_2Se [38], and $Sr_{0.06}Bi_2Se_3$ [39], in which the PHE amplitude is also three to six orders of magnitude smaller than in n-HgTe. In our comparisons, we relied on the temperature range (20–100) K and the magnetic field range (8–12) T, which is justified given the orders-of-magnitude difference in the amplitudes. Upon increasing the temperature to 150 K, the PHE amplitude decreases to ≈ 20 mOhm·cm, which is ≈ 9 times lower than $\Delta\rho$ at $T = 80$ K (Fig. 4). This value exceeds the PHE amplitude in ultra-pure HgSe [7] by a factor of ≈ 2.5. Thus, the semiclassical PHE amplitude in n-HgTe shows an ≈ 50-fold increase when the temperature is lowered by only a factor of ≈ 4 (from 150 K to 40 K). Throughout this process, the sinusoidal shape of the oscillations was well preserved.

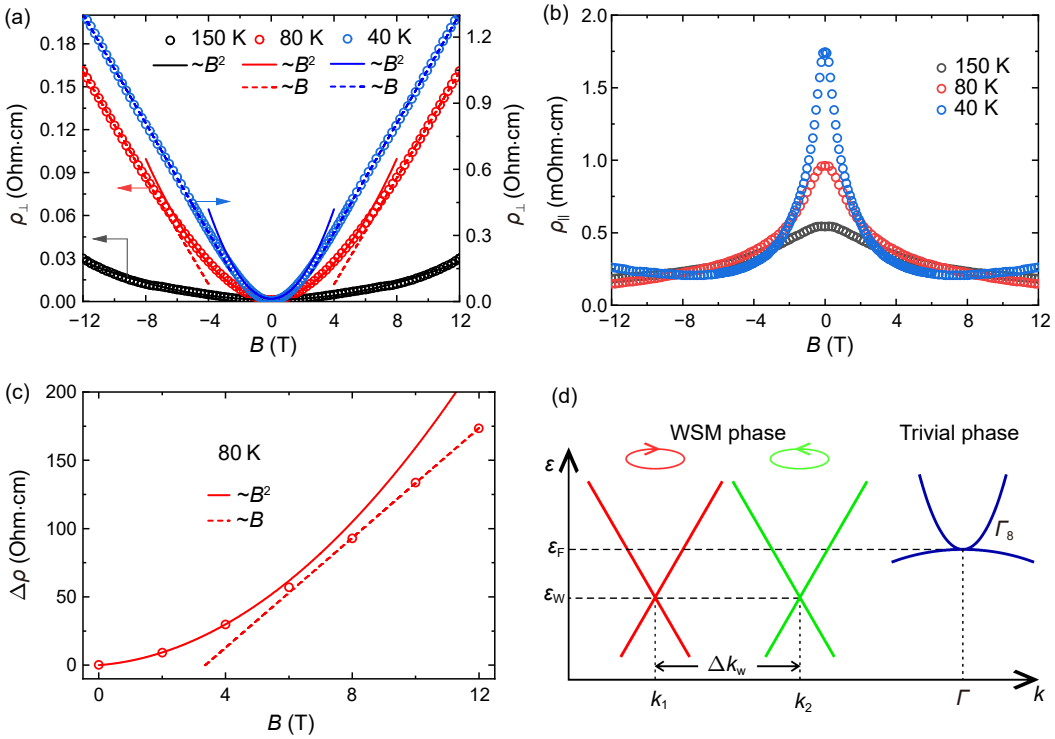

Fig. 5. (a) Magnetic field dependence of the positive transverse magnetoresistivity $\rho_\perp$ at different temperatures (symbols). Solid and dashed lines represent quadratic and linear fits, respectively. (b) Magnetic field dependence of the negative longitudinal magnetoresistivity $\rho_\parallel$ at different temperatures. (c) PHE amplitude extracted from the $\rho_{xy}(\alpha)$ fits in Fig. 2(a) (symbols), shown with quadratic (solid) and linear (dashed) fits. (d) Schematic band diagram of n-HgTe illustrating the coexistence at low energies of a trivial gapless spectrum at the Brillouin zone center and topological WSM phase. For simplicity, the latter is represented by one pair of Weyl nodes with opposite chirality, localized at k_1 and k_2 points in k-space; ε_W is the energy of the Weyl nodes; Δk_W is the separation between the Weyl nodes; ε_F is the Fermi energy at $T = 0$ relative to the Weyl nodes.

For further analysis of the PHE, we require the magnetic field dependences of $\rho_\perp(B)$ and $\rho_\parallel(B)$. These are presented in Figs. 5(a) and 5(b) at $T = 40$, 80, and 150 K. Among the measured temperatures, $\rho_\perp(B)$ increases most strongly at 40 K—by approximately three orders of magnitude at 12 T [Fig. 5(a)]—while $\rho_\parallel(B)$ shows the largest decrease (by a factor of ≈ 7) at the same temperature [Fig. 5(b)]. The ratio $\rho_\perp/\rho_\parallel \approx 7\times10^3$ then gives the MR anisotropy parameter. Evidently, such an enormous difference in the MR along and across the electric current—which implies a strong in-plane MR anisotropy in n-HgTe—results in the giant PHE amplitude at $T = 40$ K.

Let us briefly discuss possible alternative sources of anisotropy in n-HgTe. Mercury chalcogenides have been studied for more than 60 years. They are known as gapless semiconductors with an isotropic electron spectrum, in contrast to, for example, germanium, where the effective masses of charge carriers are strongly anisotropic. Therefore, the relaxation time and, consequently, the mobility are also isotropic. The electron mobility μ in the n-HgTe sample at $T = 80$ K is quite high – 8.5×10^4 cm$^2\cdot$V$^{-1}\cdot$s^{-1}. Hence, the parameter $\mu B \gg 1$ already at a field of 1 T. This implies that the classical orbital effect does not contribute to the MR change in higher fields. We note that the n-HgTe sample had a standard geometry for measuring galvanomagnetic effects (Fig. 1). At the same time, for each of V_{xx} and V_{xy}, the readings obtained from the two respective pairs of contacts (Fig. 1) differed by no more than 5%. This indicates a high uniformity of the current across the sample cross-section and the absence of current-distribution effects. Thus, standard approaches cannot account for the strong anisotropy of the planar MR in n-HgTe, nor for the fact that the PHE is accompanied by both negative longitudinal and positive transverse MRs.

The origins of the extraordinary PHE amplitude should be sought in the features of n-HgTe with an extremely low electron density, which distinguish it from other compounds. As we have demonstrated in Ref. [21], one such feature consists in the coexistence, within the band spectrum, of the topological WSM phase and a trivial (gapless) phase located at the centre of the Brillouin zone. The former can be considered responsible for the negative longitudinal MR $\rho_\parallel(B)$ due to the chiral anomaly, and the latter for the strong positive MR $\rho_\perp(B)$ without a tendency to saturation. The schematic band diagram of the n-HgTe sample with low electron density is reproduced in Fig. 5(d). The following main pieces of evidence for the existence of a WSM phase in this sample have been obtained [21]: (i) large non-saturating positive transverse MR at low temperatures, attributed to the suppression of the chirality-protected side-jump shift; (ii) observation of the CME as a direct consequence of the chiral anomaly; (iii) unconventional magnetic-field dependence of the Hall resistance in the quantum limit at $T = 0.3$ K, with signatures of Weyl-node annihilation; (iv) deviation of the $n_e(T)$ dependence from the $T^{3/2}$ law at low temperatures. In contrast, for sufficiently pure α-Sn, which is known not to be a WSM, this law holds down to the lowest T.

In accordance with the phenomenological band model [Fig. 5(d)], the Fermi level passes through the touching point of the conduction and valence bands (the charge neutrality point). The location of the Fermi level near the charge neutrality point is confirmed by the $n_e \sim T^{3/2}$ dependence in the temperature range 20–170 K, which is characteristic of an intrinsic gapless semiconductor. Moreover, at $T = 0.3$ K, an estimate gives $n_e \sim 10^{13}$ cm^{-3} [21], indicating that the Γ_8 states are depleted of charge carriers. This is precisely the key feature which leads to the formation of a perfectly compensating system of intrinsic electrons and holes at elevated temperatures. Further evidence for electron–hole compensation in this sample, established in Ref. [21], includes: (i) two-carrier Hall data fits showing that n_h exceeds n_e by only 6–18% at 80–170 K; (ii) strictly quadratic $\rho_{xx}(B)$ up to 13 T at 80 and 170 K; (iii) a crossover from quadratic to linear MR at 40 K for magnetic fields above 4 T.

Under perfect compensation, $\rho_\perp(B)$ in the bulk can become quadratic in the magnetic field provided that the contribution from the

edge regions of the sample is negligibly small [40]. Furthermore, according to theory [40], in a finite-size sample, electron–hole compensation triggers a recombination scattering mechanism, resulting in nearly linear MR. Both the quadratic and linear features of $\rho_{\perp}(B)$ are corroborated by the data in the out-of-plane configuration [21] and by the data presented in Fig. 5(a). As an independent argument, figure 5(c) shows the magnetic field dependence of the PHE amplitude $\Delta\rho$ extracted from the fitting curves of $\rho_{xy}(\alpha)$ in Fig. 2(a). In our case $\rho_{\perp} \gg \rho_{\parallel}$ at least for $B \geq 2$ T [see Figs. 5(a) and 5(b)]. Therefore, the $\Delta\rho(B)$ dependence should follow $\rho_{\perp}(B)$ in detail, as clearly demonstrated by Fig. 5(c). Thus, we conclude that the giant PHE amplitude in n-HgTe is governed by the orbital contribution $\rho_{\perp}(B)$ despite the chiral anomaly's contribution to the longitudinal MR. Evidence that the PHE originates from orbital MR rather than from the chiral anomaly has been discussed, for example, in Refs. [24, 41, 42]. On the other hand, a classic system exhibiting strong positive MR without a tendency to saturation resulting from charge compensation is WTe_2 [43]. However, as already noted, the PHE amplitude in that material is small (of the order of a few μOhm·cm). In other words, a strong transverse MR alone is insufficient for a giant PHE. Therefore, in this brief communication we do not draw definitive conclusions about the nature of the PHE in n-HgTe. Its mechanisms require further investigation, primarily involving extension of the temperature range and the use of low magnetic fields (below 2 T), where the chiral anomaly may dominate [4].

The following consideration may be of importance in this context. The band spectrum model for nominally pure n-HgTe, presented in Fig. 5(c), implies the possibility of a transformation that results in the formation of an energy gap at the Γ point of the Brillouin zone. This is feasible in solid solutions with a nonmagnetic substitutional atom (e.g., $Hg_{1-x}Cd_xTe$ [44]). In that case, the condition of perfect electron–hole compensation may be violated, resulting in a decrease of the anisotropy parameter. Therefore, HgTe-based solid solutions could, in principle, be used for achieving controllable giant PHE. The aforementioned mechanism of chirality-protected suppression of backscattering [26] should be the decisive factor in the increase of $\rho_{\perp}(B)$ in n-HgTe at sufficiently low temperatures. At such low temperatures, when the intrinsic carrier concentration becomes very small and the conductivity is governed by the Weyl cones, this mechanism fully comes into play [21]. In this regard, it is of interest to investigate the PHE in n-HgTe at fields above the quantum limit. Potentially, this sample could allow observation of the giant PHE amplitude suppression due to Weyl node annihilation in the quantum limit [28].

Conclusions

In conclusion, we report the observation of a giant planar Hall resistance and planar AMR in the n-HgTe single crystal with an extremely low electron density of 7.3×10^{14} cm^{-3}. Remarkably, the PHE amplitude at $T = 80$ K is approximately three times larger than that of the "giant PHE" we previously detected in an ultra-pure HgSe sample under identical conditions. Upon lowering the temperature to 40 K, the PHE amplitude increased further, reaching 0.9 Ohm·cm. This value is the highest ever reported for the PHE in any topological material, to the best of our knowledge. A giant PHE of unprecedented amplitude was observed in n-HgTe in a regime combining two factors—the chiral anomaly and electron–hole compensation. It is precisely electron–hole compensation that we associate with the strong transverse MR in n-HgTe; this MR mainly governs the PHE anisotropy—as in materials where the PHE originates from orbital MR. The present work primarily provides an analysis of the conditions for the appearance of the giant PHE; its nature in mercury chalcogenides requires more extensive investigation. The giant PHE observed in this unique n-HgTe sample encourages additional exploration of low-density mercury tellurides for magnetic field sensing applications, although the generality of this finding must be confirmed on other crystals. Further studies of the planar magnetotransport in the quantum limit are expected to reveal a significant suppression of the PHE in n-HgTe, associated with possible Weyl node annihilation.

Acknowlegements

Magnetotransport measurements were carried out using the equipment of the "Testing Center of Nanotechnology and Advanced Materials" Collaborative Access Center of the Institute of Metal Physics of the Ural Branch of the Russian Academy of Sciences. This work was supported by the Russian Science Foundation (Grant No. 25-22-00592).

References

[1] Goldberg C and Davis R E 1954 *Phys. Rev.* **94** 1121
[2] Thompson D A, Romankiw L T, and Mayadas A F 1975 *IEEE Trans. Magn.* **11** 1039
[3] Volovik G E 2007 *Lect. Notes Phys.* **718** 31
[4] Burkov A A 2017 *Phys. Rev. B* **96** 041110(R)
[5] Nandy S, Sharma G, Taraphder A, and Tewari S 2017 *Phys. Rev. Lett.* **119** 176804
[6] Nielsen H B and Ninomiya M 1983 *Phys. Lett. B* **130** 389
[7] Bobin S B and Lonchakov A T 2023 *JETP Lett.* **118** 495
[8] Lonchakov A T and Bobin S B 2023 *J. Phys. : Condens. Matter* **35** 065501
[9] Granell P N, Wang G, Cañon Bermudez G S, Kosub T, Golmar F, Steren L, Fassbender J, and Makarov D 2019 *npj Flexible Electronics* **3** 3
[10] Mor V, Grosz A, and Klein L 2017 *High Sensitivity Magnetometers*, Edited by Grosz A, Haji-Sheikh M J, and Mukhopadhyay S C (Springer, Cham, Switzerland), p. 201
[11] Nhalil H, Givon T, Das P T, Hasidim N, Mor V, Schultz M, Amrusi S, Klein L, and Grosz A 2019 *IEEE Sens. Lett.* **3** 8871164
[12] Nhalil H, Das P T, Schultz M, Amrusi S, Grosz A, and Klein L 2020 *Appl. Phys. Lett.* **117** 262403
[13] Lahav D, Schultz M, Amrusi S, Grosz A, and Klein L 2024 *Sensors* **24** 4384
[14] Damsgaard C D, Freitas S C, Freitas P P, and Hansen M F 2008 *J. Appl. Phys.* **103** 07A302
[15] Kim S J, Torati S R, Talantsev A, Jeon C Y, Lee S B, and Kim C G 2020 *Sensors* **20** 434
[16] Uddin S M, Sayad A, Chan J, Skafidas E, and Kwan P 2022 *Biosensors* **12** 108
[17] Bason Y, Klein L, Yau J B, Hong X, Hoffman J, and Ahn C H 2006 *J. Appl. Phys.* **99** 08R701
[18] Lee S, Bac S K, Choi S, Lee H, Yoo T, Lee S, Liu X, Dobrowolska M, and Furdyna J K 2017 *Sci. Rep.* **7** 1115
[19] Safranski C, Montoya E A, and Krivorotov I N 2019 *Nat. Nanotechnol.* **14** 27
[20] Ruan J, Jian S K, Yao H, Zhang H, Zhang S C, and Xing D 2016 *Nat. Commun.* **7** 11136
[21] Lonchakov A T, Bobin S B, Popov S D, Pryanichnikov S V, and Yakunin M V 2026 *J. Appl. Phys.* **139** 235703
[22] Yakunin M V 1988 *Fiz. Tekh. Poluprovodn.* **22** 918 [*Sov. Phys. Semicond.* **22** 1452]
[23] Lehoczky S L, Broerman J G, Nelson D A, and Whitsett C R 1974 *Phys. Rev. B* **9** 1598
[24] Liang S, Lin J, Kushwaha S, Xing J, Ni N, Cava R J, and Ong N P 2018 *Phys. Rev. X* **8** 031002
[25] Zhong J, Zhuang J, and Du Y 2023 *Chin. Phys.* **32** 047203
[26] Jiang Q D, Jiang H, Liu H, Sun Q F, and Xie X C 2016 *Phys. Rev. B* **93** 195165
[27] Kumar N, Guin S N, Felser C, and Shekhar C 2018 *Phys. Rev. B* **98** 041103(R)
[28] Zhang Q R, Zeng B, Chiu Y C, Schönemann R, Memaran S, Zheng W, Rhodes D, Chen K W, Besara T, Sankar R, Chou F, McCandless G T, Chan J Y, Alidoust N, Xu S Y, Belopolski I, Hasan M Z, Balakirev F F, and Balicas L 2019 *Phys. Rev. B* **100** 115138
[29] Cai F, Chi M, Hu Y, Liu H, Chen Y, Jing C, Ren W, and Wang H 2025

Appl. Phys. Lett. **126** 233101
[30] Li P, Zhang C, Wen Y, Cheng L, Nichols G, Cory D G, Miao G X, and Zhang X X 2019 *Phys. Rev. B* **100** 205128
[31] Xu S, Wang H, Wang X Y, Su Y, Cheng P, and Xia T L 2018 *Phys. Rev. B* **98** 195147
[32] Sonika, Hooda M K, Sharma S, and Yadav C S 2021 *Appl. Phys. Lett.* **119** 261904
[33] Singha R, Roy S, Pariari A, Satpati B, and Mandal P 2018 *Phys. Rev. B* **98** 081103(R)
[34] Vashist A, Singh R K, Wadehra N, Chakravorty S, and Singh Y 2021 *Phys. Rev. B* **104** 245121
[35] Wu M, Zheng G, Chu W, Liu Y, Gao W, Zhang H, Lu J, Han Y, Zhou J, Ning W, and Tian M 2018 *Phys. Rev. B* **98** 161110(R)
[36] Yang H, Zhou Y, Wang J, Zhou Y, Han Y, Wang J, Li Y, Zhang X, and Yang Z 2024 *Appl. Phys. Lett.* **125** 203101
[37] Bai Q, Xu M, and Li G 2025 *Mater. Today Phys.* **51** 101666
[38] Ma Y, Sun W, Xu Q, Wang X, Aqeel A, and Li G 2024 *J. Mater. Chem. C* **12** 13840
[39] Huang H, Gu J, Ji P, Wang Q, Hu X, Qin Y, Wang J, and Zhang C 2018 *Appl. Phys. Lett.* **113** 222601.
[40] Alekseev P S, Dmitriev A P, Gornyi I V, Kachorovskii V Y, Narozhny B N, Schütt M, and Titov M 2017 *Phys. Rev. B* **95** 165410.
[41] Liu Q, Fei F, Chen B, Bo X, Wei B, Zhang S, Zhang M, Xie F, Naveed M, Wan X, Song F, and Wang B 2019 *Phys. Rev. B* **99** 155119.
[42] Li Z, Xiao T, Zou R, Li J, Zhang Y, Zeng Y, Zhou M, Zhang J, and Wu W 2020 *J. Appl. Phys.* **127** 054306.
[43] Ali M N, Xiong J, Flynn S, Tao J, Gibson Q D, Schoop L M, Liang T, Haldolaarachchige N, Hirschberger M, Ong N P, and Cava R J 2014 *Nature* **514** 205.
[44] Tsidilkovski I M 1996 *Electron Spectrum of Gapless Semiconductors* (Springer Berlin, Heidelberg)